The Seismic Record
A journal of the Seismological Society of America

On the Importance of Using Directional Information in the Search for Lower Mantle Reflectors

Federica Rochira*[1] and Christine Thomas[1]

Abstract

The *SS* precursor signals are a powerful tool for mapping topography of mantle discontinuities, which are sensitive to the thermal and compositional structure of the mantle. The depth of mantle discontinuities is usually estimated using the differential travel time between the main arrival and its precursor. However, this method ignores potential travel path deviations that influence the travel time of precursor signals. Here, we use an approach that considers directivity information as well as travel-time measurements. Applying seismic array techniques, we measure slowness, back azimuth, and travel time of the signals, and use this information to backproject to the point of reflection. In our test dataset, we observe deviations from the predicted values in slowness and back azimuth in the range of 0.1–2.3 s/° and 1–20°, respectively. These values lead to reflection locations that can differ considerably from theoretical reflection points calculated with great circle plane paths as well as depths different from the depth calculated for in-plane propagation, with differences up to ~150 km. Our results indicate that the travel-path deviations should be considered to avoid misinterpretation of mantle discontinuities and potentially reduce previously observed scatter in discontinuity depth.

Cite this article as Rochira, F. and C. Thomas (2023). On the Importance of Using Directional Information in the Search for Lower Mantle Reflectors, *The Seismic Record*. **3**(**2**), 96–104, doi: 10.1785/0320220038.

Supplemental Material

Introduction

Maps of seismic discontinuities in the mantle provide useful information about its thermal and compositional state. For instance, the main discontinuities in the mantle transition zone, that is, the 410 and 660 km discontinuities, are due to phase transitions in the olivine system, which, in turn, are sensitive to the lateral temperature and chemical variations in the mantle (e.g., Deuss, 2009). Additional discontinuities have been detected in the mantle, although they are not necessarily globally observed, and their origin is less well constrained, such as the 210 km discontinuity (e.g., Rost and Weber, 2001), the discontinuity at 520 km depth (e.g., Shearer, 2000), and increasing evidence of reflectors detected around 1000 km depth (Jenkins *et al.*, 2017; Waszek *et al.*, 2018). Up to date, there are still considerable dissimilarities about the depth of mantle discontinuities, which, in turn, lead to different interpretations in terms of thermal and compositional structure of the mantle (Houser *et al.*, 2008; Deuss, 2009).

Several methodologies have been used to sample mantle discontinuities, such as triplications, receiver functions, and *ScS* reverberations (Deuss, 2009, and references therein). Perhaps the most commonly used method is based on *PP* and SS precursors, which are underside reflections (Fig. 1a) from seismic discontinuities that travel a similar path to the main *PP* and *SS* phase but arrive earlier (e.g., Shearer, 2000; Deuss, 2009). The measured differential travel time between the main arrival and its precursor is used to estimate the discontinuity depth, using a standard Earth model. However, such an approach ignores potential travel-path deviations that may affect the travel time

1. Institut für Geophysik, Westfälische Wilhelms-Universität Münster, Münster, Germany, https://orcid.org/0000-0003-0456-3065 (FR); https://orcid.org/0000-0002-7845-5385 (CT)

*Corresponding author: rochira@uni-muenster.de

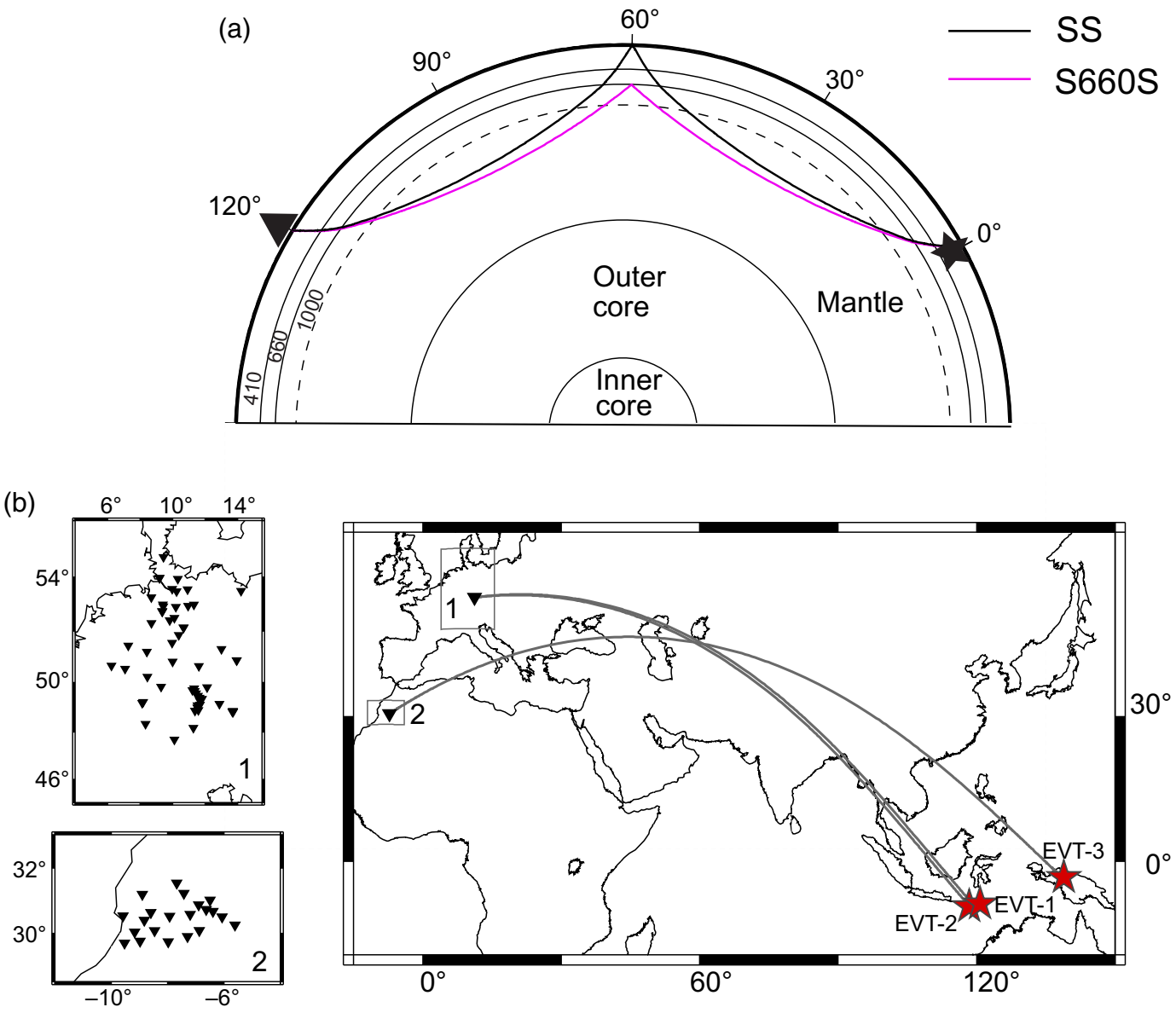

Figure 1. (a) Ray paths of an *SS* wave (reflected at the surface) and the precursor reflecting off the 660 km mantle discontinuity, halfway between the source (black star) and the receiver (black triangle). (b) Locations of sources (red stars) and arrays (black triangles) used in this study. Great circle paths are shown as gray lines. The numbered insets refer to the locations of the center of the arrays displayed on the left side: German Regional Seismic Network (GRSN) and Gräfenberg (GRF) array (1); and Münster–Morocco and Bristol–Morocco array (2).

of precursor signals, and thus the calculation of depth and location of the reflector.

The previous studies have questioned the accuracy of this approach, showing, for instance, how the complex structure of the Fresnel zone of the underside reflections can result in artefacts leading to erroneous discontinuity depths (Chaljub and Tarantola, 1997; Neele *et al.*, 1997; Neele and de Regt, 1999). Other studies focused on the influence of mantle heterogeneities on precursor travel time and on the accuracy of the travel-time corrections for wavespeed anomalies (e.g., Zhao and Chevrot, 2003). Zheng and Romanowicz (2012) show with 3D waveform modeling that upper mantle heterogeneities near the receiver side, that is, far away from the reflection point, can generate artificial precursors (e.g., double $S^{660}S$ precursors) that are sometimes also observed in real data, and may lead to misinterpretations as double discontinuities or complex

structure in the bounce point region. Koroni and Trampert (2016), finally, tested the reliability of linearized ray theory for converting travel times of *SS* precursors to discontinuity depths. Their results show that the location of uplifts and depressions of the discontinuities are correctly identified, although the amplitude of the topography is considerably underestimated.

Here, we use an approach that considers not only travel times but also directivity parameters, that is, back azimuth and slowness, which provide information on the horizontal angle measured clockwise from north and the inclination of the wavefront approaching the array, respectively. We then use this information to backtrace the detected signals to their location of reflection.

This methodology has previously been used for detecting out-of-plane signals to map the presence of reflectors and scatterers in the lower mantle (e.g., Schumacher and Thomas, 2016; Rochira *et al.*, 2022), and investigating other phenomena often associated with back-azimuth deviations, for example, multipathing and diffraction at velocity gradient boundaries (e.g., Ward *et al.*, 2020). Here, we extend the methodology to *SS* precursors that are commonly thought to travel on the great circle path. Because path deviations generate travel-time deviations, we test how much such path deviations contribute to variations in estimated reflection point locations and depths.

Processing and Observations

To investigate the mantle beneath Eurasia, we search for *SS* waves and precursors (Fig. 1a) that originate from a discontinuity at depth *d*, that is, S^dS waves (e.g., Rost and Weber, 2001). For this, we use events with focal depths shallower than 75 km and epicentral distance between 100° and 140° to avoid precursor depth phases and topside reflections that interfere with the precursory wavefield (Schmerr and Garnero, 2006; Schmerr and Thomas, 2011). Because this study is presenting a proof of concept, we are not analyzing all possible events but show the effects of path deviations on reflection locations on three selected events chosen for their high quality and visibility of precursors. The great circle paths for these three different events are shown in Figure 1b. Events 1 and 2 are events from Indonesia, recorded at the German Regional Seismic Network (GRSN), whereas event 3 is occurred in Indonesia recorded at the temporary Münster–Morocco and Bristol–Morocco arrays presented in Figure 1b (see Tables S1, S2, available in the supplemental material to this article, for details about sources and receivers). The complete dataset will be analyzed in a follow-up study.

The S^dS precursor arrivals are difficult to identify on single seismic recordings due to their weak amplitude, which is only a few percent of the main *SS* amplitude (e.g., Deuss, 2009; Lessing *et al.*, 2015). We, therefore, use seismic array techniques (Rost and Thomas, 2002, and references therein) to detect potential precursor signals. In array methods, the seismic traces are shifted and summed according to the "delay and sum" method that amplifies coherent phases with the appropriate slowness, and suppresses phases with different slowness or incoherent noise. After applying a second-order butterworth band-pass filter with corner periods of 15 and 75 s to the data, we calculate fourth-root vespagrams (Rost and Thomas, 2002, and references therein) to identify precursors based on their slowness and travel time, using the theoretical back azimuth of the reference station. Figure 2a,c,e shows the vespagrams for each of the events displayed in Figure 1b. In particular for event 1, two potential precursor signals are detected, labeled (1) and (2) in Figure 2a, but their slowness and travel time do not match the predicted slowness and travel time of the $S^{1000}S$ or $S^{660}S$ phases. When using the observed travel time and the ak135 model (Kennett *et al.*, 1995), the depths of the reflection points are estimated to be at 872 km (1) and 722 km (2), respectively, without taking slowness and back azimuth into account. Furthermore, the time window matching the travel time for the $S^{410}S$ shows no coherent signal in the vespagram. Conversely, the vespagram for event 2 shows a precursor signal arriving in the time window matching the travel time of the $S^{1000}S$, but again no coherent signals with the appropriate travel time and slowness of the predicted $S^{660}S$ and $S^{410}S$ arrival (Fig. 2c). Finally, the vespagram for event 3 shows four potential precursor signals whose travel times approximately match the predicted travel times of the $S^{1000}S$, $S^{660}S$, $S^{520}S$, and $S^{210}S$ (Fig. 2e). Similar to events 1 and 2, the time window around the travel time for $S^{410}S$ shows no coherent signal.

To verify the detected signals and to gain information on the travel path, we perform a sliding window slowness–back-azimuth analysis (Rost and Weber, 2001; Rost and Thomas, 2002, 2009) using a time window of 20 s, starting 60 s before the first arrival (S_{diff}) up to 60 s after the predicted *SS* arrival time. The analysis window is shifted across the trace every 5 s, and slowness and back azimuth are measured simultaneously using a slowness range of 6–18 s/° (with a step of 0.1 s/°), and a back-azimuth range of ±50° (with a step of 1°) from the direction of the great circle path. Examples of slowness–back-azimuth diagrams are shown in Figure 2b,d,f for the events 1, 2, and 3, respectively. Because slowness and back azimuth are

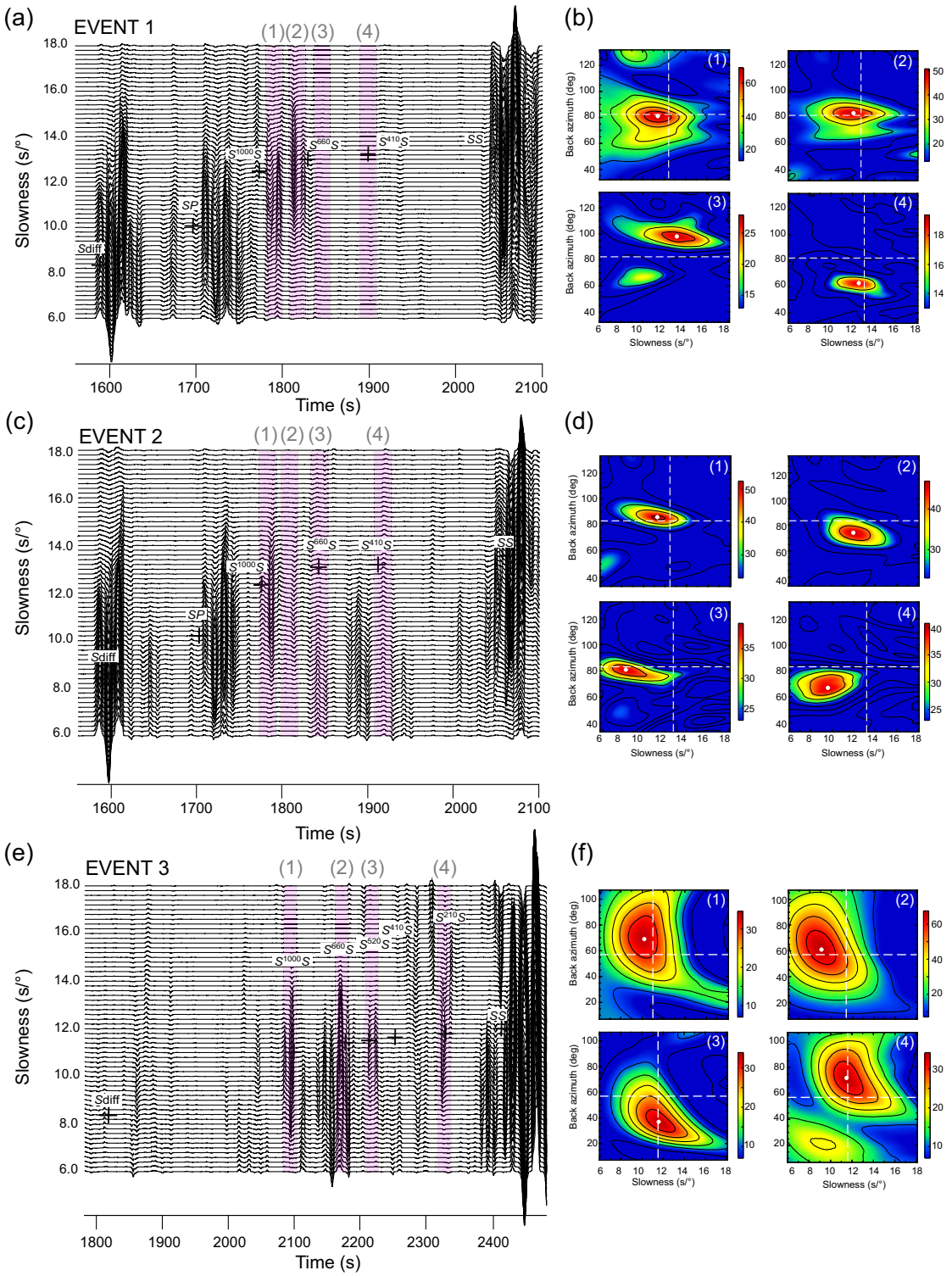

Figure 2. (a,c,e) Fourth-root vespagrams computed with the theoretical back azimuth for events 1, 2, and 3, respectively. The crosses mark the theoretical slowness and travel times of the labeled phases assuming the ak135 velocity model, except for the phases labeled $S^{1000}S$ and $S^{520}S$ for which a modified ak135 model is used. Data are filtered with a second-order butterworth band-pass filter and corner periods of 15 and 75 s. The pink areas in the vespagrams indicate the time window of 20 s for slowness–back-azimuth analysis shown on the right side. (b,d,f) Slowness–back-azimuth diagrams for the time windows labeled 1, 2, 3, 4 in (a,c,e). The color bar indicates the fourth-root beamform energy. Horizontal and vertical white dashed lines correspond to the theoretical back azimuth and slowness, respectively. White circles mark the observed slowness and back azimuth for each arrival. Note that the amplitudes in the vespagrams are amplified by a factor of (a,c) 50 and (e) 100.

interconnected, a change in back azimuth likely generates a change in slowness as well; therefore, we search also for arrivals whose slowness is different from theoretical predictions.

Carrying out the analysis, we observe deviations in slowness and back azimuth compared to predicted values for our detected precursors. On average we find deviations in slowness of 0.9 s/° and 8° in back azimuth. Moreover, with the slowness–back-azimuth analysis we are able to detect signals that travel out of plane and thus are invisible when using the theoretical back azimuth in the stacking processing (see also Rost and Thomas, 2002; Schumacher and Thomas, 2016). For example, $S^{410}S$ signals for events 1 and 2, labeled (4) in Figure 2a–d are detected, which were not visible in the vespagrams (Fig. 2a,c). No arrivals other than the ones shown in Figure 2 had slowness–back-azimuth values similar to predicted *SS* precursors. Some had very different values such as arrival (3) in Figure 2d, and they are likely not precursor arrivals, because their slowness is too low for an *S*-to-*S* reflection.

If a signal is clearly visible in the slowness–back-azimuth diagram, we measure the absolute travel time of the arrival in the fourth-root beam trace for the measured slowness using the observed back azimuth and also confirm it in linear stacks. A backtracing algorithm is then used to locate the reflection point for each of the detected precursor arrival. A grid search is implemented to find the location of reflector that best fits the observed travel time, given the measured directivity parameters (see also Schumacher and Thomas, 2016 for more information). Because errors in slowness, back azimuth, and travel time present uncertainties in relocating the reflectors, we follow Schumacher and Thomas (2016) and Rochira *et al.* (2022), and calculate the standard deviation for slowness and back azimuth using the amplitude values deviating less than 10% from the maximum amplitude of the observed signal in the slowness–back-azimuth analysis (white circle in Fig. 2b,d,f). We also estimate an uncertainty in travel-time picking of 10 s, considering the dominant period of our signals and the time window used for the slowness–back-azimuth analysis. The errors differ between events due to the array design and aperture.

Calculated Reflection Points

For all precursor signals detected in the three events, we observe deviations in slowness of 0.1–2.3 s/° and in back azimuth of 1°–20° (Fig. 2). Differently to the previous studies relying on travel time alone when estimating the depth of mantle discontinuities and assuming that the waves travel along the great circle path direction, we take the information on the observed slowness and back azimuth of the detected signals, as well as the measured travel time into account. Using the backtracing algorithm we find locations and depths as displayed in Figure 3a,c,e, Figure S1, and given in Table 1.

Because the detected signals deviate from the great circle path, the estimated locations of the bounce points (displayed as ellipses in Fig. 3a,c,e) also differ compared with the predicted locations halfway between source and receiver on the great circle path (black crosses in Fig. 3a,c,e). Differences in distances between the backtraced and predicted bounce points are in the range of ∼8°–21° (Table 1). Even considering the horizontal uncertainties in locating reflectors (size of ellipses in Fig. 3a,c,e), due to errors in measuring back azimuth (on average ± 3.7°) and slowness (on average ± 0.67 s/°), the locations of reflectors do not match the predicted locations of the bounce points. For comparison of the effect of using directional information and travel time, we have calculated the depth of the reflectors, assuming that the waves travel in plane, that is, using the predicted slowness and back azimuth and the observed travel time of the precursor signals. The results are displayed in the maps in Figure 3b,d,f, and details for each bounce point are provided in Table 1. In addition, the locations vary slightly in the great circle plane due to varying travel time.

The maps (Fig. 3) show that, in addition to affecting the location of reflectors, travel-path deviations also influence the calculated depth of reflectors. The *SS* waves are minimum-maximum phases (Neele *et al.*, 1997), and any deviations from the midpoint between source and receiver will lead to travel-time variations. Using the backtracer, we determine the reflection depth and find that there are strong differences in depths between the two methods in the range of ∼28 km up to 157 km (Table 1).

As noted earlier, precursor signals for $S^{410}S$ are not detected in our events when using vespagrams alone but when performing slowness–back-azimuth analyses, events 1 and 2 show signals with a different back azimuth whose travel time matches that of an $S^{410}S$ phase and which can be backprojected with an *S*-to-*S* reflection. Their reflection depths, however, are much deeper and shallower than 410 km, respectively. For event 3, we do not find a coherent signal in the time window of the $S^{410}S$ signal. Interestingly, most of the detected precursors in our dataset do not match the depths of the mantle discontinuities at 410, 520, and 660 km depth, suggesting that they could be reflected at other structures in the mantle (Schumacher and Thomas, 2016; Rochira *et al.*, 2022). Finally, arrival (3) for event 2 cannot be backprojected with an *S*-to-*S* wave due to its very low slowness.

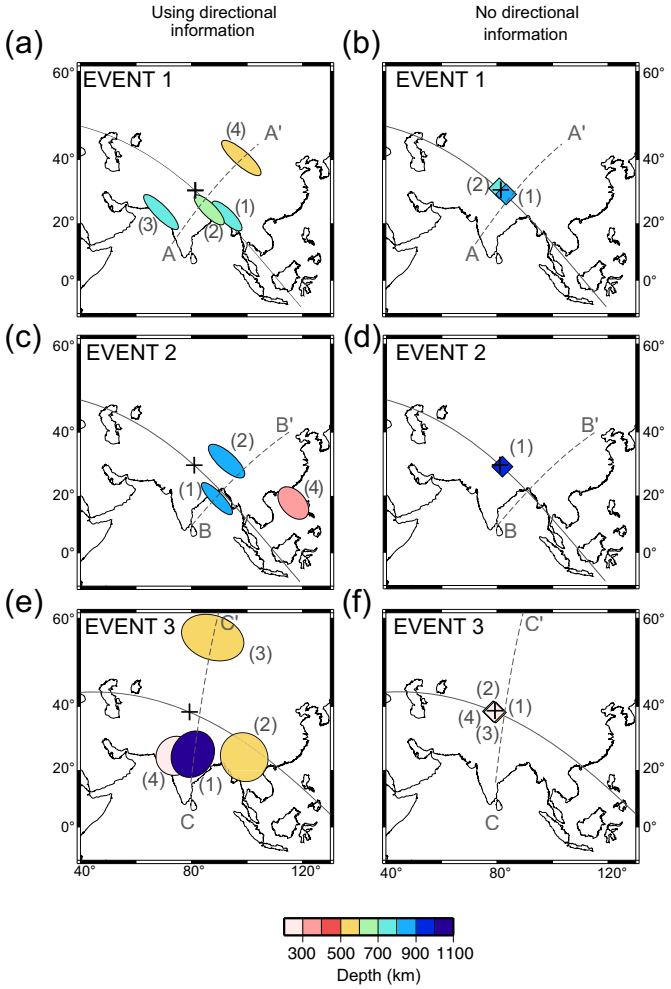

Figure 3. Geographical positions of reflectors detected in this study displayed as (a,c,e) ellipses and as (b,d,f) diamonds for (a,b) event 1, (c,d) event 2, and (e,f) event 3. (a,c,e) Results using directional information (observed back azimuth and slowness) and (b,d,f) results assuming waves travel along the great circle path (predicted back azimuth and slowness). The size of each ellipse is related to the uncertainties in back azimuth and slowness measurements. The color scale gives the depth of reflectors. Black crosses on the maps denote the predicted location of *SS* reflection points at the surface. Numbered labels as in Figure 2. Note that only the bounce points for precursors visible in the vespagrams in plane (Fig. 2a,c,e) are shown in panels (b,d,f). Great circle paths are shown as solid gray lines. Dashed gray lines indicate the profiles of the cross sections displayed in Figure S1.

To evaluate the influence of deviations for each measured parameter (back azimuth, slowness, and time) on the estimated depth and location of the bounce points we conduct a synthetic test: starting from the values of slowness, back azimuth, and travel time for the S^dS phase for event 1, computed for a 1D Earth model (Kennett *et al.*, 1995), we determine locations and depths of the bounce points, using the backtracing algorithm and vary only one of the three input parameters at a time. In particular, we change the back-azimuth values in the range of ±2°–10° using steps of 2°, slowness values vary from ±0.2 to ±1 s/° using steps of 0.2 s/°, and travel time varies between ±2 and 10 s with steps of 2 s. Figure S2 shows the results for the $S^{1000}S$ phase, and similar results are found for the $S^{410}S$ and $S^{660}S$ phases. Small deviations in back azimuth (up to 4°) yield differences in latitude and longitude of up to ∼2° with respect to the predicted values, whereas bigger back-azimuth deviations (up to 10°) generate differences in geographical coordinates of up to ∼7°. Differences in depths are on the order of 2–10 km for small back-azimuth deviations and up to ∼60 km for bigger deviations. A similar trend is observed for small deviations in slowness (up to 0.4 s/°) with discrepancies in latitude and longitude of up to ∼3° and up to ∼10 km in depth. On the other hand, bigger slowness deviations (up to 1 s/°) determine differences in geographical coordinates of up to ∼9° and up to ∼70 km in depth. Travel-time deviations produce the smallest deviations in latitude and longitude with less than 1°, while primarily affecting the depth of the reflection point, with differences from ∼10 to ∼60 km.

Discussion

Contrary to the common approach of mapping depths of mantle discontinuities using differential travel-time measurements between the main phase and its precursor (e.g., Shearer, 2000; Schmerr and Garnero, 2006; Deuss, 2009), we adopt a strategy that also considers directivity information to infer depth and location of the detected reflectors. Our results show that there can be a marked difference between the estimated reflection points in both location and depth between the two methods; but the difference is small when the precursors travel on the great circle path. Several previous studies tested for path deviations before using the precursor travel times (e.g., Saki *et al.*, 2015) and if in-plane waves are used, then estimated depths will be more reliable. There may still be errors in depth estimation due to various reasons such as the influence of the tomography model used to correct for travel times (Schmerr and Garnero, 2006; Koroni and Trampert, 2016), additional mantle heterogeneities (Zheng and Romanowicz, 2012), the influence of the complicated Fresnel zone of the *SS* waves (Chaljub and Tarantola, 1997; Neele *et al.*, 1997), noise, and array configuration or plane wavefront assumption (Ward *et al.*, 2021).

Since the deviations in slowness and back azimuth also change the location of the reflection points, as shown in

Table 1
List of the Signals Observed in This Study and Backtraced to Their Reflection Points

Event	Array	Observed Signal Parameters				Bounce Point (Using Observed u, θ, Travel Time)			Bounce Point (Using Observed Travel Time and Predicted u, θ)			Difference between Bounce Point Locations		
1	2	3	4	5	6	7	8	9	10	11	12	13	14	15
Nr	Nr	u (s/°)	θ (°)	Travel Time (s)	Nr	Latitude (°)	Longitude (°)	h (km)	Latitude (°)	Longitude (°)	h (km)	Δh (km)	ΔDis (°)	ΔDis (~km)
1	1	11.4	81	1793	1	22.52	92.81	780	29.67	83.29	872	92	11.14	1078
1	1	12.1	84	1821	2	24.62	86.42	694	31.54	80.86	722	28	8.48	838
1	1	13.2	98	1843	3	24.03	68.95	719	–	–	–	–	–	–
1	1	12.6	63	1899	4	40.36	98.14	569	–	–	–	–	–	–
2	1	11.3	86	1785	1	19.32	89.24	857	29.67	81.87	944	87	12.32	1177
2	1	12	74	1810	2	31.5	92.72	839	–	–	–	–	–	–
2	1	8.4	81	1855	3	–	–	–	–	–	–	–	–	–
2	1	9.6	67	1914	4	17.57	116.75	310	–	–	–	–	–	–
3	2	10.2	69	2091	1	25.21	80.34	1075	38.5	78.61	1043	32	13.37	1240
3	2	9.1	61	2165	2	25.25	97.59	545	38.62	78.26	702	157	21.08	2115
3	2	11.6	37	2217	3	56.05	87.71	599	38.29	79.26	514	85	18.63	1891
3	2	11.5	72	2320	4	24.77	74.22	258	38.47	78.7	217	41	14.22	1522

The second row of the table indicates the column number. Columns 1 and 2 indicate the source (as given in Table S1) and array (see Table S2). Columns 3–6 indicate the observed slowness, back azimuth, travel time, and reference number of each signal as used in Figure 2. Columns 7–9 provide the latitude, longitude, and depth of the backprojected bounce point, taking into account the observed directional parameters, as well as the measured travel time. Columns 10–12 provide latitude, longitude, and depth of the bounce point located using the theoretical slowness and back azimuth, and the observed travel time. Column 13 provides the absolute difference in depth calculated using the depth values in columns 9 and 12. Columns 14 and 15 give the absolute difference in distance, in degree, and in kilometers, respectively, between the bounce points, using the coordinates values in columns 7–9 and 10–12. Nr, number; u, slowness; θ, back azimuth; h, depth; Δh, difference in depth; and ΔDis, difference in distance.

Figure 3, Figure S1, and Table 1, mapping depths to the theoretical reflection point may also lead to erroneous estimates of topography, and subsequently misleading interpretation of mantle temperature and mineralogy, because topography of mantle discontinuities is influenced by these. Previous works showed a large scatter for the seismic reflector at 1000 km depth (e.g., Waszek *et al.*, 2018) and also for other discontinuities (e.g., Chambers *et al.*, 2005; Deuss *et al.*, 2006; Thomas and Billen, 2009). Contribution of compositional variations in aluminum or iron, and the presence of water or melt have been proposed to explain the discrepancies in topography of the mantle discontinuities observed in several previous studies (e.g., Chambers *et al.*, 2005; Deuss *et al.*, 2006; Thomas and Billen, 2009). Our results show that using directional information instead of relying only on travel-time measurements can provide an alternative explanation for such discrepancies.

Moreover, it is usually assumed that the differential travel time between the main phase *SS* and its precursor is only sensitive to the structure between the discontinuity depth and the surface (e.g., Deuss, 2009). This implies that the potential heterogeneities, such as structure or topography beneath the station, or structures in the source region should deviate paths of both the waves in the same way. In contrast, we observe smaller deviations for *SS* waves than for precursors (Fig. S3) with maximum deviations in slowness and back azimuth for the *SS* waves of 0.4 s/° and 4°, respectively. This suggests that either the same heterogeneities deviate the paths of the main phase and its precursor differently, which is unlikely, given the almost same paths and frequency of the waves, or other structurers are responsible for the bigger deviations observed for mantle discontinuity reflected precursors. Should topography be present at a reflector, following Snell's law, the reflection of a seismic wave at the nonhorizontal parts of the reflector likely happens outside the great circle path, whereas the surface reflected *SS* wave would likely not be affected much (e.g., Lessing *et al.*, 2015), which can explain the difference.

In addition, our analysis shows that, when using slowness–back-azimuth analysis, we are able to detect precursor signals that travel out of plane but are not visible when using the theoretical back azimuth in the stacking process (e.g., $S^{410}S$ in Fig. 2). Therefore, if topography is present at the discontinuity, this might contribute to the lack of detection of precursors observed in the previous studies, which was also attributed to several mechanisms such as a reduced velocity contrast at the discontinuity, interference with other seismic arrivals, or local lateral variations in mineralogy (Lessing *et al.*, 2015, and references therein). A systematic search for arrivals could help to detect more underside reflections off mantle discontinuities, especially in the presence of discontinuity topography and perhaps help to distinguish effects from topography from those of other discontinuity properties. Finally, this approach might be also useful for detecting precursors to other seismic phases (e.g., *PP* and $P'P'$) or investigating other phenomena such as multipathing and diffraction (Ward *et al.*, 2021).

Conclusion

We use array methods to detect *SS* precursors, and measure their direction (slowness and back azimuth) and travel time. We observe deviations in slowness and back azimuth for the precursor signals compared with the predicted values that are in the range between 0.1–2.3 s/° and 1°–20°, respectively. Backtracing, using slowness, back azimuth, and travel time, to the position and depth of the reflector, we find that the location of the bounce points differs considerably compared with the predicted location. When backprojecting with directional information and travel times, the depths of the reflector differ compared with depths estimated using only travel time. The results show that some of the observed scatter of discontinuity depth could be due to path effects, and the approach may help to better understand properties of mantle reflectors, such as topography. Furthermore, an incorrect estimation of the depth and location of reflectors may contribute to a misleading interpretation of mantle discontinuities. Therefore, we suggest that the travel-path deviations should be considered in future work to better constrain the geographical position and the depth of mantle reflectors.

Data and Resources

Data were downloaded using ObsPy—a python toolbox for seismology (Krischer *et al.*, 2015) from the data center at the Incorporated Research Institutions for Seismology (IRIS) and Bundesanstalt für Geowissenschaften und Rohstoffe (BGR), and DOI numbers are given in Table S2. The Supplemental Material for this article includes three additional figures and two tables providing details on the events and networks used.

Declaration of Competing Interests

The authors declare that there are no conflicts of interest recorded.

Acknowledgments

The authors would like to thank the editors Keith Koper and Jessica Irving, and the reviewers Daniel Frost and Jamie Ward

for helpful suggestions and comments that improved the clarity of the article. The authors thank Lina Schumacher for providing the code for backtracing the signals. The data were analyzed with Seismic Handler (Stammler, 1993) and the TauP toolkit (Crotwell *et al.*, 1999). Maps were drawn with the Generic Mapping Tools (GMT; Wessel and Smith, 1995). The study was financed by the bilateral ANR-DFG TIMEleSS project (ANR-17-CE31-0025, TH1530/18-1, SA2585/3-1, and SP1216/8-1) and the bilateral PROCOPE-PPP program (PHC 40555PC and DAAD 57390184). The authors acknowledge support from the Open Access Publication Fund of the University of Münster.

References

Chaljub, E., and A. Tarantola (1997). Sensitivity of SS precursors to topography on the upper-mantle 660-km discontinuity, *Geophys. Res. Lett.* **24,** no. 21, 2613–2616.

Chambers, K., J. H. Woodhouse, and A. Deuss (2005). Topography of the 410-km discontinuity from PP and SS precursors, *Earth Planet. Sci. Lett.* **235,** 610–622.

Crotwell, H. P., T. J. Owens, and J. Ritsema (1999). The TauP Toolkit: Flexible Seismic Travel-time and Ray-path Utilities, *Seismol. Res. Lett.* **70,** 154–160.

Deuss, A. (2009). Global observations of mantle discontinuities using SS and PP pre-cursors, *Surv. Geophys.* **30,** nos. 4/5, 301–326.

Deuss, A., S. A. T. Redfern, K. Chambers, and J. H. Woodhouse (2006). The nature of the 660-kilometer discontinuity in Earth's mantle from global seismic observations of PP precursors, *Science* **311,** 198–201.

Houser, C., G. Masters, M. Flanagan, and P. Shearer (2008). Determination and analysis of long-wavelength transition zone structure using SS precursors, *Geophys. J. Int.* **174,** 178–194.

Jenkins, J., A. Deuss, and S. Cottar (2017). Converted phases from sharp 1000 km depth heterogeneity beneath Western Europe, *Earth Planet. Sci. Lett.* **459,** 196–2017.

Kennett, B. L. N., E. R. Engdahl, and R. Buland (1995). Constraints on seismic velocities in the Earth from travel times, *Geophys. J. Int.* **122,** 108–124.

Koroni, M., and J. Trampert (2016). The effect of topography of upper-mantle discontinuities on SS precursors, *Geophys. J. Int.* **204,** 667–681.

Krischer, L., T. Megies, R. Barsch, M. Beyreuther, T. Lecocq, C. Caudron, and J. Wassermann (2015). ObsPy: A bridge for seismology into the scientific python ecosystem, *Comp. Sci. Disc.* **8,** 014003, doi: 10.1088/1749-4699/8/1/014003.

Lessing, S., C. Thomas, M. Saki, N. Schmerr, and E. Vanacore (2015). On the difficulties of detecting PP precursors, *Geophys. J. Int.* **201,** 1666–1681.

Neele, F., and H. de Regt (1999). Imaging upper-mantle discontinuity topography using underside-reflection data, *Geophys. J. Int.* **137,** 91–106.

Neele, F., H. de Regt, and J. VanDecar (1997). Gross errors in upper-mantle discontinuity topography from underside reflection data, *Geophys. J. Int.* **129,** 194–204.

Rochira, F., L. Schumacher, and C. Thomas (2022). Mapping the edge of subducted slabs in the lower mantle beneath southern Asia, *Geophys. J. Int.* **230,** 1239–1252.

Rost, S., and C. Thomas (2002). Array seismology: Methods and applications, *Rev. Geophys.* **40,** no. 3, 1008, doi: 10.1029/2000RG000100.

Rost, S., and C. Thomas (2009). Improving seismic resolution through array processing techniques, *Surv. Geophys.* **30,** 271–299.

Rost, S., and M. Weber (2001). A reflector at 200 km depth beneath the northwest Pacific, *Geophys. J. Int.* **147,** 12–28.

Saki, M., C. Thomas, S. E. J. Nippress, and S. Lessing (2015). Topography of upper mantle seismic discontinuities beneath the North Atlantic: The Azores, Canary and Cape Verde plumes, *Earth Planet. Sci. Lett.* **409,** 193–202.

Schmerr, N., and E. Garnero (2006). Investigation of upper mantle discontinuity structure beneath the central Pacific using SS precursors, *J. Geophys. Res.* **111,** no. B8, B08305, doi: 10.1029/2005JB004197.

Schmerr, N., and C. Thomas (2011). Subducted lithosphere beneath the Kuriles from migration of PP precursors, *Earth Planet. Sci. Lett.* **311,** 101–111.

Schumacher, L., and C. Thomas (2016). Detecting lower-mantle slabs beneath Asia and the Aleutians, *Geophys. J. Int.* **205**, 1512–1524.

Shearer, P. M. (2000). Upper mantle seismic discontinuities, *Geophysical Monograph-AGU*, Vol. 117, 115–132.

Stammler, K. (1993). Seismichandler–Programmable multichannel data handler for interactive and automatic processing of seismological analyses, *Comput. Geosci.* **19,** 135–140.

Thomas, C., and M. Billen (2009). Mantle transition zone structure along a profile in the SW Pacific: Thermal and compositional variations, *Geophys. J. Int.* **176,** 113–125.

Ward, J., A. Nowacki, and S. Rost (2020). Lateral velocity gradients in the African lower mantle inferred from slowness space observations of multipathing, *Geochem. Geophys. Geosys.* **21,** e2020GC009025 , doi: 10.1029/2020GC009025.

Ward, J., M. Thorne, A. Nowacki, and S. Rost (2021). Automatic slowness vector measurements of seismic arrivals with uncertainty estimates using bootstrap sampling, array methods and unsupervised learning, *Geophys. J. Int.* **226,** 1847–1857.

Waszek, L., N. C. Schmerr, and M. D. Ballmer (2018). Global observations of reflectors in the mid-mantle with implications for mantle structure and dynamics, *Nat. Commun.* **9,** 385, doi: 10.1038/s41467-017-02709-4.

Wessel, P., and W. H. F. Smith (1995). New version of the generic mapping tools, *Eos Trans. AGU* **76,** 329–329.

Zhao, L., and S. Chevrot (2003). SS-wave sensitivity to upper mantle structure: implications for the mapping of transition zone discontinuity topographies, *Geophys. Res. Lett.* **30,** no. 11, 1590.

Zheng, Z., and B. Romanowicz (2012). Do double 'SS precursors' mean double discontinuities? *Geophys. J. Int.* **191,** 1361–1373.

Manuscript received 9 November 2022
Published online 18 April 2023